Rheology and microstructure of non-colloidal suspensions under shear studied with Smoothed Particle Hydrodynamics

Adolfo Vázquez-Quesada, Marco Ellero

PII: S0377-0257(15)00218-9
DOI: 10.1016/j.jnnfm.2015.12.009
Reference: JNNFM 3728

To appear in: *Journal of Non-Newtonian Fluid Mechanics*

Received date: 30 October 2015
Revised date: 19 December 2015
Accepted date: 22 December 2015

Please cite this article as: Adolfo Vázquez-Quesada, Marco Ellero, Rheology and microstructure of non-colloidal suspensions under shear studied with Smoothed Particle Hydrodynamics, *Journal of Non-Newtonian Fluid Mechanics* (2015), doi: 10.1016/j.jnnfm.2015.12.009

Highlights

- A threedimensional SPH model of non-colloidal suspensions is presented.
- The scheme avoids the use of small time steps for divergent lubrication forces.
- Rheology of the system is studied for volume fractions up to 0.5.
- Results are compared with available simulation and experimental data.
- Close agreement with the experiments is obtained for volume fractions up to 0.35.

Rheology and microstructure of non-colloidal suspensions under shear studied with Smoothed Particle Hydrodynamics

Adolfo Vázquez-Quesada[1], Marco Ellero[2]

Zienkiewicz Centre for Computational Engineering (ZCCE), Swansea University, Bay Campus, Swansea SA1 8QQ, United Kingdom.

Tel.: +44 (1792) 295514

Dedicated to Professor Roger I. Tanner on his 82nd Birthday

Abstract

In this work a Smoothed Particle Hydrodynamics model is presented to study rheology and microstructure of a non-colloidal suspension of spherical particles in a Newtonian solvent. The scheme presented in [X. Bian, M. Ellero, Comput. Phys. Commun. 185 (1) (2014) 53-62.] is extended to three-dimensions incorporating both normal and tangential short-range interparticle lubrication forces which are solved implicitly with a refined splitting strategy. The scheme allows to bypass prohibitively small time steps generally required for handling divergent lubrication forces and allows to simulate large particle systems. Rheology of a three-dimensional hard-spheres suspension confined in a plane Couette rheometer is investigated for concentrations up to $\phi = 0.5$. Results for the relative suspension viscosity η_r are analyzed against sample size and numerical convergence of the splitting lubrication scheme and compared with available experimental and simulations data. Very close agreement with the experiments is obtained for η_r up to $\phi = 0.35$. At larger concentrations, our results are still unable to explain the significant viscosity increase observed in experiments. Modest shear-thickening is also observed which is related to anisotropy of the

[1]A.Vazquez-Quesada@swansea.ac.uk
[2]M.Ellero@swansea.ac.uk

particle radial distribution function (RDF) and presence of reversible hydrodynamic aggregates increasing in size with increasingly applied shear rates.

Keywords: Non-colloidal suspensions, Rheology, Smoothed Particle Hydrodynamics

1. Introduction

Rheology and dynamics of particles suspended in simple and complex media represent both a relevant technical issue and an enormous theoretical challenge. Important industrial applications involve for example pipeline transport of slurries, processing of filled plastics, ceramics and drilling mud for oil recovery but also much of our daily-life products in cosmetic, pharmaceutics and food industry deal with complex suspensions of particles [1, 2]. In the oil and gas industry, for example, colloidal or non-colloidal particles, such as clays or asphaltenes are typically used for the extraction of hydrocarbons [3] and as a component of water-based drilling fluids [4]. On the other hand, particulate systems with complex rheological response have allowed to design recently novel smart materials and gels with desired target properties [5, 6]. Under real processing conditions, geometrical confinement is also a critical aspect as it can trigger flow instabilities in concentrated suspensions [7, 8, 9], altering rheo-dynamical response and playing an essential role in several operations as for example in dispensing material through a narrow nozzle, e.g. in ink-jet technologies [10]. It is therefore critical to understand, predict and control accurately suspension rheology for a wide range of systems and under different external conditions in order to target practical industrial demand.

Suspension characterization is conventionally done via rheological experiments aiming at the measurement of viscosity and normal stresses under controlled viscometric conditions. Mono-dispersed solid spheres suspended in a Newtonian medium represent possibly the simplest test-case. However, despite its apparent simplicity, it is remarkable that even this system is still far from being completely understood. Several analytical derivations for the suspension

viscosity η as function of particle volume fraction ϕ exist, starting from the Einstein's formula [11, 12] in the dilute regime, to approximate theories [13, 14] and semi-empirical expressions [15] at large concentrations. However, for a complete understanding of the link between suspension microstructure and bulk rheology, numerical simulations represent a powerful complementary tool to theory and experiment. In the past decades several techniques have been developed and applied successfully to simulation of colloidal and non-colloidal suspensions. Examples include Finite Element Methods [16, 17], Lattice Boltzmann methods [18, 19], Dissipative Particle Dynamics (DPD) [20, 21, 22, 23, 24] and the Stokesian Dynamics [25, 26, 27, 28, 29, 30, 31, 32].

Despite their usefulness however, one of the most serious drawbacks generally involves predictive capability, being numerical simulations in most cases restricted to qualitative or at best semi-quantitative agreement. In the context of non-colloidal suspensions for example, no current numerical method is able to date to show accurate quantitative agreement with experimental data for the effective relative suspension viscosity as a function of the solid volume fraction [33, 34, 35], with best data [27, 32] still underestimating experiments by over 40 % at moderate concentrations. In these experiments solid particles of size in the range $10 - 100\mu$m are typically used allowing to reach Peclet numbers in excess of 10^7 for which Brownian motion is practically not relevant [35].

Also significant shear-thinning was observed experimentally in these studies for non-colloidal systems already at moderate ϕ [33, 35, 9]. Despite this phenomenon has been known for a long time [36, 37], it is quite remarkable that no simulation is currently capable to predict it and a physical explanation for it is still missing. Note that this problem is not related to the shear-thinning behavior occurring in Brownian colloidal suspensions (small Peclet numbers) which is well understood in terms of an equilibrium/non-equilibrium transition in the microstructure [2].

A non-colloidal suspension can be regarded as the infinite Peclet number limit of colloidal system. Based on this analogy recently Cwalina et al. compared their high-shear rates viscometric data for a suspension using 260nm-

radius silica nanoparticles [38] with data for non-Brownian systems. Results for the relative suspension viscosity agree very well with non-colloidal data of Nott et al. [34]. Despite the good agreement in the systems investigated in [38] shear-thickening (as opposite to shear-thinning) is typically observed at high shear rates, which appears to be related, at least in its "continuous" manifestation, to formation of transient reversible hydrodynamics aggregates, termed "hydroclusters" [39, 28, 27, 2, 40]. The idea behind hydrocluster theory is that upon increasing shear rate, convective forces dominate over entropic repulsive Brownian forces, being able to bring particles close together forming large hydrodynamic aggregates. In the thin gaps between particles inside hydroclusters, diverging lubrication forces are active which in turn induce larger stresses in the system. The existence of hydroclusters is confirmed by experiments [41, 42, 40] flow-small angle neutron scattering [43, 41, 42], optical methods including flow dichroism [41], fast confocal microscopy [40] and numerical simulations [39, 28, 27]. Very recently highly accurate measurement of non-equilibrium microstructure through the shear thickening transition using small angle neutron scattering (SANS) measurements was presented in [44].

With regarding to the suspension rheology, it is worth to notice that different experimental systems -colloidal/non-colloidal- exhibiting very different rheological responses still appear to deliver relative viscosity data which agree extraordinary well together. As mentioned above quantitative agreement with these data cannot be reached to date with available numerical techniques.

In relation to this point, it should be also remarked that, in order to reproduce numerically the higher viscosities observed in experiments, and "discontinuous" shear-thickening -i.e. a sudden jump (as opposite to continuous mild rise) in suspension viscosity- some authors have introduced in their models also frictional forces acting between particles -in addition to lubrication contributions [45, 46, 31, 47]. It is expected that for sufficiently high concentrations particles become so close that contacts among them happen, increasing therefore the system viscosity. Despite this approach has allowed to reproduce the observed discontinuous shear thickening behavior in dense suspensions [45, 46, 31], the

effect of the roughness in the viscosity still does not match the experimental results [48]. Moreover, deviations between simulation results and experimental data appear already in moderately concentrated case, significantly below the jamming transition, where the system would reach frustration and granular dynamics governed by frictional contacts is expected to dominate.

In the present work numerical simulations of suspensions of non-colloidal spherical particles confined between two planar walls under shear flow have been performed using Smoothed Particle Hydrodynamics (SPH) [49], a Lagrangian meshless method where flow fields are represented by means of co-moving fluid volumes interacting via pairwise forces. Given the local nature of the method, SPH enjoys a high degree of parallelization [50] enabling direct High Performance Computing applications (HPC).

We extend here the scheme presented initially in [51, 52] to three-dimensional cases and incorporate, beside normal also tangential contributions to short-range interparticle lubrication forces. In fact it was recently showed that normal lubrication contributions alone under-predict suspension viscosity [53] and does not allow to reach accurate agreement with available simulation data [27, 32]. A refined splitting strategy presented here allows to handle simultaneously all the contributions of the diverging lubrication forces implicitly, bypassing the need of prohibitively small numerical time steps and allowing to simulate large particle-systems. More importantly, implicit iteration allows to control accurately the residual error in the numerical integration of the lubrication dynamics and to check convergence on viscometric properties.

Advantages of using this technique include also the possibility in the future to study rheology of (i) suspension of arbitrary-shape suspended particles [51] or confining geometries; (ii) incorporation of Brownian effects -i.e. via Smoothed Dissipative Particle Dynamics (SDPD) [54, 55, 51] - as well as (iii) non-Newtonian effects of the suspending phase [56, 57].

The structure of the paper is as follows: a brief introduction of the SPH model for the description of the suspending phase is outlined in section 2.1. The non-colloidal suspension model is described in section 2.2 where interaction fluid-

solid and lubrication forces between suspended solid particles are also described. In section 2.3 the modified splitting scheme for the implicit integration of the full set of lubrication forces is presented in detail. Finally, in section 3 numerical results are presented. In particular, the dynamics of two hydrodynamically-interacting spherical particles undergoing a shear flow is described in Sec. 3.1 Afterwards, the rheology (Sec. 3.2) and microstructure (Sec. 3.2.1) of a many-particle system confined and shared in a plane Couette rheometer is investigated for concentrations up to $\phi = 0.5$. Results of the suspension viscosity and microstructure are reported for systems with $N \geq 3000$ suspended hard spheres and for Couette gap to particle radius ratio up to $L_z/a = 64$ which is comparable to common experimental setups [35, 30]. Conclusion and final discussion are finally reported in section 4.

2. The suspension model

In this section the details of the model are presented, separately, for the solvent medium and for the suspended solid particles.

2.1. The SPH model for the suspending fluid

SPH is a meshless Lagrangian fluid model where the Navier-Stokes equations are discretized using a set of points denoted as fluid particles. Positions and momenta of every fluid particle (labelled by Latin indices $i = 1, .., N$) evolve in a Lagrangian framework, according to the SPH discrete equations.

$$\dot{\boldsymbol{r}}_i = \boldsymbol{v}_i \tag{1}$$

$$m\dot{\boldsymbol{v}}_i = -\sum_j \left[\frac{P_i}{d_i^2} + \frac{P_j}{d_j^2}\right] \frac{\partial W(r_{ij})}{\partial r_{ij}} \boldsymbol{e}_{ij} + \sum_j (D+2)\eta_0 \left[\frac{1}{d_i^2} + \frac{1}{d_j^2}\right] \frac{\partial W(r_{ij})}{\partial r_{ij}} \frac{\boldsymbol{e}_{ij} \cdot \boldsymbol{v}_{ij}}{r_{ij}} \boldsymbol{e}_{ij} \tag{2}$$

where D is the number of dimensions of the system, P_i the pressure of particle i, $\boldsymbol{e}_{ij} = \boldsymbol{r}_{ij}/r_{ij}$ the unit vector joining particles i and j, $\boldsymbol{v}_{ij} = \boldsymbol{v}_i - \boldsymbol{v}_j$ their velocity

difference and η_0 the viscosity of the solvent. $d_i = \sum_j W(r_{ij}, r_{cut})$ is the number density associated to particle i estimated as a weighted interpolation with a bell-shaped function W with compact support r_{cut} [54]. With this definition, mass conservation and continuity equations for the mass density $\rho_i = m d_i$ (m particle mass) are implicitly satisfied, whereas the Newton's equations of motion (2) for the particles are a discrete representation of the momentum Navier-Stokes equation in a Lagrangian framework, with the first summation in Eq. (2) representing the pressure gradient term and second summation corresponding to the Laplacian of the velocity field. Advantage of these SPH equations over alternative choices is that both linear and angular momentum are exactly conserved [58], which is a critical requirement to reproduce accurately the dynamics of freely-translating/rotating solid particles in a fluid medium [51]. For the weighting function W, the present work adopts a quintic spline kernel [59] with cutoff radius $r_{cut} = 4\,dx$ (dx being the mean fluid particle separation) where accurate velocity fields and drag data were obtained in [60]. Finally, in order to close the equations of motion an equation of state for the pressure is used relating it to the estimated local mass density, i.e. $P_i = p_0[(\rho_i/\rho_0)^\gamma - 1] + p_b$, where the input parameters ρ_0, p_0 and γ are chosen to have a liquid speed of sound $c_s = \sqrt{\gamma p_0/\rho_0}$ sufficiently larger than any other velocity present in the problem, therefore enforcing approximate incompressibility [61] and p_b is a background pressure.

2.2. Solid particles: fluid-structure interaction

Solid inclusions of arbitrary shape can be modelled using boundary particles similar to fluid ones, located inside the solid region [51] (Fig. (1)). Boundary particles interact with fluid particles by means of the same SPH forces described in Eq. (2). No-slip boundary condition at the liquid-solid interface is enforced during each interaction between fluid particle i and boundary particle j by assigning an artificial velocity to the boundary particle j, which satisfy zero interpolation at the interface [59]. The same approach is also used to model any arbitrary wall. Once all the forces acting on every boundary particle j belonging

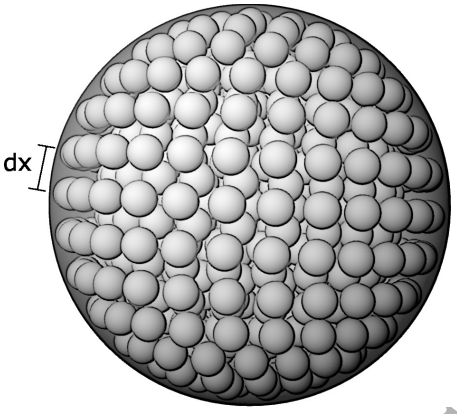

Figure 1: Scheme of the location of the boundary particles (white spheres) within a solid sphere. The resolution is 5 boundary particles per radius and corresponds to that used in this study.

to a solid domain (labelled by Greek indexes α) are calculated, the total force $\boldsymbol{F}_\alpha^{\rm sph}$ and torque $\boldsymbol{T}_\alpha^{\rm sph}$ exerted by the surrounding fluid modelled by SPH can be obtained as

$$\boldsymbol{F}_\alpha^{\rm sph} = \sum_{j\in\alpha} \boldsymbol{F}_j, \qquad \boldsymbol{T}_\alpha^{\rm sph} = \sum_{j\in\alpha} (\boldsymbol{r_j} - \boldsymbol{R}_\alpha) \times \boldsymbol{F}_j \tag{3}$$

where $\boldsymbol{R}_\alpha$ is the center of mass of the solid particle α (Fig.1). When properly integrated, $\boldsymbol{F}_\alpha^{\rm sph}$ and $\boldsymbol{T}_\alpha^{\rm sph}$ allow to obtain the new linear velocity $\boldsymbol{V}_\alpha$, angular velocity $\boldsymbol{\Omega}_\alpha$ and position of the solid inclusion. Positions of boundary particles inside α are finally updated according to a rigid body motion [53].

2.3. Normal/tangential lubrication force between solid particles

The present SPH model captures accurately the long range hydrodynamic interactions (HIs) between solid particles [51]. As discussed in detail in [52, 53] when two solid particles (e.g. α and β) get very close to each other, the HIs mediated by the SPH fluid are poorly represented and need to be corrected. In [53] we have considered an analytical solution for the pairwise short-range HIs obtained in the limit of small sphere's separation and superimposed it to the

far-field multi-body SPH HIs. In [53] a standard choice for short-range normal hydrodynamic force (denoted as lubrication force), i.e. directed along the vector $\boldsymbol{e}_{\alpha\beta}$ joining the centers of mass of solid particles α and β was adopted, that reads $\boldsymbol{F}^{\rm lub}_{\alpha\beta}(s) = -6\pi\eta_0 \left(\frac{a_\alpha a_\beta}{a_\alpha + a_\beta}\right)^2 \frac{1}{s} \left(\boldsymbol{V}_{\alpha\beta} \cdot \boldsymbol{e}_{\alpha\beta}\right) \boldsymbol{e}_{\alpha\beta}$ where $\boldsymbol{V}_{\alpha\beta}$ is their relative velocity, a_α and a_β their radii and s is the distance in the gap between sphere-sphere surfaces. This expression was motivated by the fact the it represents the leading order term in the analytical solution for lubrication, i.e. diverging as $\mathcal{O}(1/s)$ for s $\to 0$. Although, the normal lubrication model was able to reproduce accurately the dynamics of two solid spheres approaching each other in a quiescent fluid and interacting under a constant shear flow [53], it was noticed that values of total suspension viscosity for a multi-particle system were visibly smaller than those obtained using previous numerical techniques, e.g. Stokesian Dynamics [27, 32]. In order to address this problem, in this work we extend the lubrication HIs between solid particles incorporating higher-order contributions according to [62]. The new terms introduce corrections of $\mathcal{O}(1/\ln(s))$ in the normal lubrication force but also new tangential forces acting between the spheres arise, as follows:

$$\begin{aligned} \boldsymbol{F}^n_{\alpha\beta}(s) &= f_{\alpha\beta}(s) \boldsymbol{V}_{\alpha\beta} \cdot \boldsymbol{e}_{\alpha\beta} \boldsymbol{e}_{\alpha\beta} \\ \boldsymbol{F}^t_{\alpha\beta}(s) &= g_{\alpha\beta}(s) \boldsymbol{V}_{\alpha\beta} \cdot (\boldsymbol{1} - \boldsymbol{e}_{\alpha\beta} \boldsymbol{e}_{\alpha\beta}) \end{aligned} \tag{4}$$

where the scalar functions $f_{\alpha\beta}(s)$ and $g_{\alpha\beta}(s)$ are defined as

$$\begin{aligned} f_{\alpha\beta}(s) &= -6\pi\eta \left[\left(\frac{a_\alpha a_\beta}{a_\alpha + a_\beta}\right)^2 \frac{1}{s} + a_\alpha \left(\frac{1 + 7\frac{a_\beta}{a_\alpha} + \left(\frac{a_\beta}{a_\alpha}\right)^2}{5\left(1 + \frac{a_\beta}{a_\alpha}\right)^3} \right) \ln\left(\frac{a_\alpha}{s}\right) \right] \\ g_{\alpha\beta}(s) &= -6\pi\eta a_\alpha \left[\frac{4\frac{a_\beta}{a_\alpha}\left(2 + \frac{a_\beta}{a_\alpha} + 2\left(\frac{a_\beta}{a_\alpha}\right)^2\right)}{15\left(1 + \frac{a_\beta}{a_\alpha}\right)^3} \right] \ln\left(\frac{a_\alpha}{s}\right) \end{aligned} \tag{5}$$

As discussed in [52, 53], when simulating two spheres moving towards each other with constant velocity, the normal hydrodynamic force acting on them and computed uniquely from the SPH discretization of the suspending fluid deviates from the divergent behavior predicted by the theory typically at a gap

distance equal to half cutoff $s_c^n = r_{cut}/2$ and remains approximately constant at smaller distances. When using the normal lubrication force at distances below s_c^n, the constant SPH force contribution should be removed [19, 52] from Eq. (4) in order to obtain a well-defined and accurate transition between the far/short range HIs. The normal lubrication correction force reads therefore

$$\boldsymbol{F}_{\alpha\beta}^{n,corr}(s) = \begin{cases} \boldsymbol{F}_{\alpha\beta}^{n}(s) - \boldsymbol{F}_{\alpha\beta}^{n}(s_c^n), & \text{if } s < s_c^n \\ \\ 0, & \text{if } s \geq s_c^n \end{cases} \tag{6}$$

In the first graph of Fig. 2 the correction of the normal lubrication applied to a SPH simulation of two equal particles of radius $a = a_\alpha = a_\beta = 1$ approaching each other with equal and opposite velocities $V = \pm 1$ and immersed in a quiescent solvent characterized by a viscosity $\eta_0 = 8.46$, a speed of sound $c_s = 30$ and a density $\rho_0 = 1$, is compared to the force obtained without any correction. The corresponding particle Reynolds number for this flow is $\mathrm{Re} = aV_\alpha\rho_0/\eta_0 \approx 0.1$ and the Mach number Ma=0.03. The size of the simulation box is $L_x = L_y = L_z = 16a$ and the number of computational particles in each direction is $N_x = N_y = N_z = 80$. The cutoff radius of the SPH kernel is $r_{cut} = 0.8a$. Periodic boundary conditions are considered in every direction. It has been checked that the size of the box is big enough to avoid periodicity effects on the following results. For comparison, the merged theoretical solution between the close and far field approaches calculated in [63] is used. As it can be seen, the correct normal HI is reproduced at every interparticle distance.

A similar argument can be applied to the tangential component of the lubrication in the case of two particles moving perpendicular to their center lines. Unlike the normal component, in this case it is found that the distance where SPH-mediated HIs fail to predict the theoretical solution is approximately $s_c^t = r_{cut}/8$ and therefore the tangential lubrication correction is applied for $s < s_c^t$ as follows

$$\boldsymbol{F}_{\alpha\beta}^{t,corr}(s) = \begin{cases} \boldsymbol{F}_{\alpha\beta}^{t}(s) - \boldsymbol{F}_{\alpha\beta}^{t}(s_c^t), & \text{if } s < s_c^t \\ \\ 0, & \text{if } s \geq s_c^t \end{cases} \tag{7}$$

Comparison between the SPH force with and without tangential lubrication correction is shown in the second graph of Fig. 2. Again good agreement is obtained over the entire range of interparticle distances s.

It should be remarked that, beside short-range lubrication forces, additional repulsive forces acting between solid particles are introduced to stabilize simulations and prevent solid particle penetrability which might occur, especially in the case of highly concentrated multi-particle suspensions. They read [64, 65].

$$\boldsymbol{F}^{\mathrm{rep}}_{\alpha\beta} = F_0 \frac{\tau e^{-\tau s}}{1 - e^{-\tau s}} \boldsymbol{e}_{\alpha\beta} \tag{8}$$

where τ^{-1} determines the range of the repulsive force, and F_0 its magnitude.

2.3.1. Semi-implicit integration scheme for lubrication

Since the lubrication force (4) is divergent at vanishing separation, integration of the solid particle equations of motion will pose a serious time-step limitation when an explicit scheme is used. In [52, 53] we have proposed an efficient implicit splitting scheme to integrate accurately and stably singular normal lubrication forces between nearly contacting solid spheres. In this work we generalize this strategy to both normal and tangential components. In order to calculate the evolution of the solid particles from time step n to $n+1$, the exerted forces on the solid particles are split in several contributions. First, for every solid particle, velocities are updated explicitly according to the long-range hydrodynamic force $\boldsymbol{F}^{\mathrm{sph}}_{\alpha}$ exerted by the SPH fluid particles, i.e.

$$\boldsymbol{V}'_{\alpha} = \boldsymbol{V}^{n}_{\alpha} + \boldsymbol{F}^{\mathrm{sph}}_{\alpha} \Delta t / m_{\alpha} \tag{9}$$

where m_α is the mass of the particle α. After this step, the integration of the short-range lubrication forces are considered. As mentioned above, an explicit method is not suitable for treating the lubrication force, especially in very concentrated suspensions, because of the small time steps required. In order to deal with this problem, the following splitting integration scheme is used. Collecting Eqs. (4), (6) and (7) we can write the total lubrication correction force

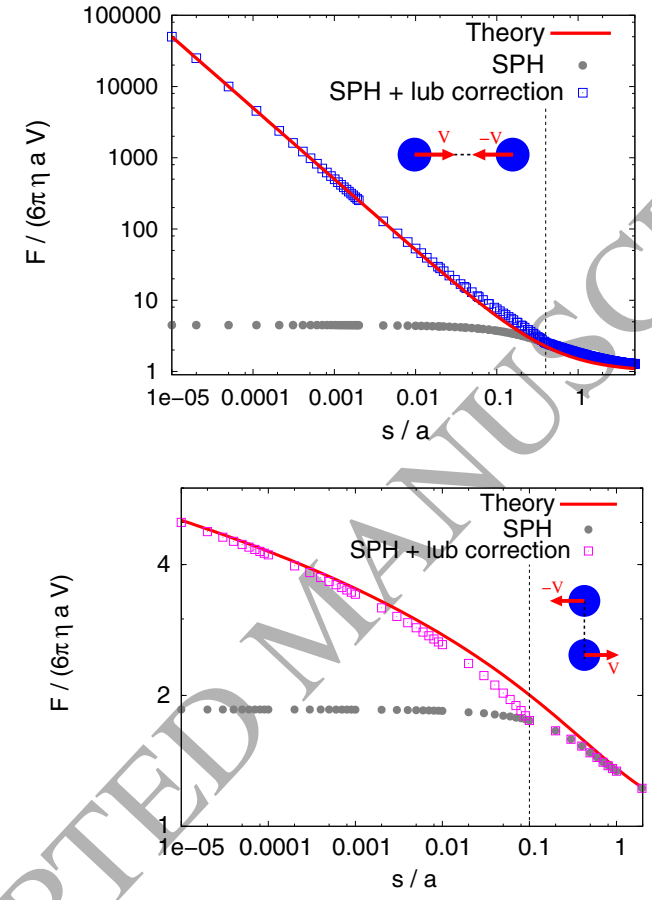

Figure 2: Overall hydrodynamic force acting between two equal spheres ($a_\alpha = a_\beta = a = 1$) moving with constant relative velocity $\boldsymbol{V}_{\alpha\beta}$ approaching along center-to-center line $\boldsymbol{e}_{\alpha\beta}$ (top graph), or perpendicular to their center-to-center line (bottom graph): theoretical curves are obtained from [63]. SPH results before and after correction using Eqs. (6) and (7) are shown. Dashed vertical lines determine the distances where lubrication correction is activated (at $s_c^n = r_{cut}/2 = 0.4a$ for the normal case and at $s_c^t = 0.1a$ for the tangential one).

incorporating both normal and tangential terms as

$$\begin{aligned} \boldsymbol{F}^{corr}_{\alpha\beta}(s) &= \boldsymbol{F}^{n,corr}_{\alpha\beta}(s) + \boldsymbol{F}^{t,corr}_{\alpha\beta}(s) \\ &= \boldsymbol{V}_{\alpha\beta}\left\{\left[f_{\alpha\beta}(s) - f_{\alpha\beta}(s^n_c)\right]\left[1 - H(s - s^n_c)\right]\boldsymbol{e}_{\alpha\beta}\boldsymbol{e}_{\alpha\beta} + \right. \\ &\quad \left. \left[g_{\alpha\beta}(s) - g_{\alpha\beta}(s^t_c)\right]\left[1 - H(s - s^t_c)\right]\left[\mathbf{1} - \boldsymbol{e}_{\alpha\beta}\boldsymbol{e}_{\alpha\beta}\right]\right\} \end{aligned} \tag{10}$$

where H is the Heaviside step function. The time step Δt is split in N_{sweep} substeps of size $\Delta t_{sweep} = \Delta t / N_{sweep}$. For every pair of solid particles α and β, their velocities are updated pair-wisely and implicitly from the following system of equations

$$\begin{aligned} \tilde{\boldsymbol{V}}_{\alpha} &= \boldsymbol{V}'_{\alpha} + \tilde{\boldsymbol{F}}^{corr}_{\alpha\beta}(s)\Delta t_{sweep}/m_{\alpha} \\ \tilde{\boldsymbol{V}}_{\beta} &= \boldsymbol{V}'_{\beta} - \tilde{\boldsymbol{F}}^{corr}_{\alpha\beta}(s)\Delta t_{sweep}/m_{\beta} \end{aligned} \tag{11}$$

Given that $\tilde{\boldsymbol{F}}^{corr}_{\alpha\beta}$ is a linear function of $\tilde{\boldsymbol{V}}_{\alpha\beta}$, Eqs.(11) are a linear system of six unknowns, which can be reduced to three when the conservation of linear momentum between pairs of particles is considered. More importantly, no numerical inversion of matrices is needed, since a solution of Eqs.(11) can be obtained analytically. This is done by subtracting the second equation of (11) to the first one, which after simple rearrangement, gives

$$\tilde{\boldsymbol{V}}_{\alpha\beta} \cdot \left[\left(B_{\alpha\beta} - A_{\alpha\beta}\right)\boldsymbol{e}_{\alpha\beta}\boldsymbol{e}_{\alpha\beta} + \left(1 - B_{\alpha\beta}\right)\mathbf{1}\right] = \boldsymbol{V}'_{\alpha\beta} \tag{12}$$

with $A_{\alpha\beta}$, $B_{\alpha\beta}$ defined as

$$\begin{aligned} A_{\alpha\beta} &= \begin{cases} \left[f_{\alpha\beta}(s) - f_{\alpha\beta}(s^n_c)\right]\Delta t_{sweep}\left[\frac{1}{m_\alpha} + \frac{1}{m_\beta}\right], & \text{if } s < s^n_c \\ 0, & \text{otherwise} \end{cases} \\ B_{\alpha\beta} &= \begin{cases} \left[g_{\alpha\beta}(s) - g_{\alpha\beta}(s^t_c)\right]\Delta t_{sweep}\left[\frac{1}{m_\alpha} + \frac{1}{m_\beta}\right], & \text{if } s < s^t_c \\ 0, & \text{otherwise} \end{cases} \end{aligned} \tag{13}$$

The solution to this system can be obtained by inverting the matrix of the system. This is done by considering that its structure is of the form $[Y_{\alpha\beta}\mathbf{1} + Z_{\alpha\beta}\boldsymbol{e}_{\alpha\beta}\boldsymbol{e}_{\alpha\beta}]$

where $Y_{\alpha\beta}$ and $Z_{\alpha\beta}$ are functions to be determined. The solution is

$$\tilde{\boldsymbol{V}}_{\alpha\beta} = \left(\frac{1}{1-B_{\alpha\beta}}\right)\boldsymbol{V}'_{\alpha\beta}\cdot\left[\mathbf{1}+\left(\frac{A_{\alpha\beta}-B_{\alpha\beta}}{1-A_{\alpha\beta}}\right)\boldsymbol{e}_{\alpha\beta}\boldsymbol{e}_{\alpha\beta}\right] \tag{14}$$

Given that linear momentum conservation must be held, individual velocities of the particles are finally calculated as

$$\tilde{\boldsymbol{V}}_{\beta} = \frac{m_\alpha\left(\boldsymbol{V}'_\alpha - \tilde{\boldsymbol{V}}_{\alpha\beta}\right)+m_\beta\boldsymbol{V}'_\beta}{m_\alpha+m_\beta} \qquad \tilde{\boldsymbol{V}}_{\alpha} = \tilde{\boldsymbol{V}}_{\alpha\beta}+\tilde{\boldsymbol{V}}_{\beta} \tag{15}$$

In conclusion, implicit solution of pairwise lubrication interaction is estimated in one step and it can be repeated very efficiently for all the possible pairs of solid particles interacting via lubrication.

In order to control this parameter, an adaptive criterion is adopted: we perform one default number of sweeps $N_{sweep} = 2^m$ and another one with $N_{sweep} = 2^{m-1}$. Difference between the solid particle velocities $\{\tilde{\boldsymbol{V}}_\alpha\}$ obtained from the two loops is measured by a non-dimensionalized L_2 norm

$$e^m = \frac{\sqrt{\sum_{\alpha=1}^{N}\left(\tilde{V}_\alpha^m - \tilde{V}_\alpha^{m-1}\right)^2}}{\sqrt{\sum_{\alpha=1}^{m}\left(\tilde{V}_\alpha^m\right)^2}} \tag{16}$$

and compared with a predefined tolerance ϵ. Numerical convergence is obtained after a prescribed N_{sweep} which is changed dynamically during the simulation to guarantee $e^m < \epsilon$. For the typical value of $\epsilon = 10^{-2}$ chosen in this work, an averaged number of 2-3 iterations per time step is sufficient for convergence. For details about the iteration loop and improved performance, see Ref.[52].

Finally, once the implicit splitting scheme has been applied for normal and tangential lubrication interactions, repulsive forces between solid particles are considered. Given that it is an interaction depending only on the position, a Verlet Scheme [52] is used.

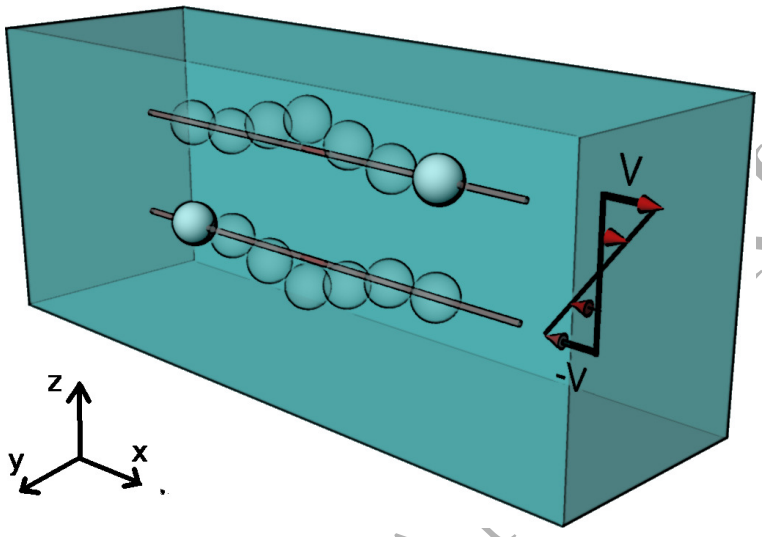

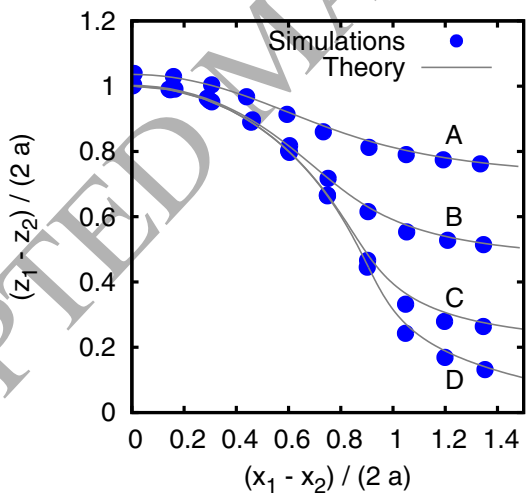

Figure 3: Top: sketch of the simulations of two particle in a shear flow. and rotating in a uniform shear flow. Bottom: comparison of the SPH results (dots) with the Batchelor's analytical solution (solid lines) [13] for different initial conditions.

3. Numerical results

3.1. Trajectories of two spheres in a constant shear flow

In this section, the trajectories of two solid spheres embedded in a liquid under uniform shear flow (Fig. 3, top) are considered and compared to the analytical solutions of Batchelor [13]. Both spheres have identical radii a and simulation box size is $L_x = L_y = 8a, L_z = 16a$. In x and y directions periodic boundary conditions are considered. However in this case, two parallel walls are placed at the upper/lower boundaries of the box in the z direction. In order to produce a uniform shear flow, the two walls are moving in opposite direction with velocities $\pm V_w$. Again, it has been checked that the size of the box is large enough to avoid effects of the walls and the periodic boundaries on the final particle trajectories. Both, viscosity and speed of sound are taken as in Sec. 2.3, whereas the shear rate now is $\dot{\gamma} = 2V_w/L_z = 0.053$. The tolerance of the splitting implicit integrator is taken as $\epsilon = 0.01$. Comparisons of the simulated trajectories with the analytical Batchelor's results are given in the Fig. 3 (bottom) showing very close agreement for all the initial conditions considered.

3.2. Suspension rheology

In this section we consider a suspension of solid spheres of radius a confined between two parallel walls and study its viscometric behaviour under constant shear. Particle concentration is defined as $\phi = 4\pi N_c a^3/3V$ where $V = L_x \times L_y \times L_z$ is the total volume of the simulation box and N_c is the number of solid particles. In Fig. 4 a snapshot for domain size $V = 32a \times 32a \times 32a$ is depicted. Box sizes corresponding to $V = 16a \times 8a \times 64a$ have been also considered to test finite size effects.

As in Ref.[53], a shear rate is applied to the sample by moving upper and lower planar walls with equal and opposite velocities $\pm V_w$. Unlike ideal bulk systems, e.g. simulated using Lees-Edwards boundary conditions, a sheared confined suspension might exhibit a small amount of slip at the walls. As a

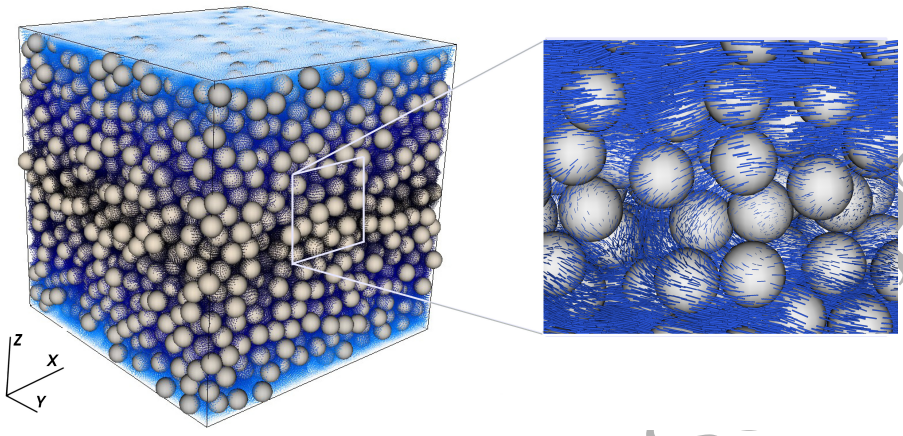

Figure 4: Snapshot of a simulation corresponding to solid concentration $\phi = 0.4$, and box size $L_x = 32a, L_y = 32a, L_z = 32a$. Total number of solid particles was $N_c = 3129$ and SPH fluid particles $N \approx 4.3 \times 10^6$. Solid and fluid particles have been drawn with grey and blue colors respectively. In the inset, blue lines correspond to velocity vectors associated to SPH fluid particles. For clarity, upper/lower walls have not been drawn.

consequence, the input shear rate defined as $\dot{\gamma}^{in} = 2V_w/L_z$ might be slightly different to the real shear rate effectively experienced by the suspension. In order to take into account this effect, similarly to experiments, we estimate an effective shear rate $\dot{\gamma}$ measured by interpolating the linear velocity profile in the bulk region [66], therefore eliminating possible artifacts due to wall slip.

From $\dot{\gamma}$ and from the component σ_{xz} of the shear stress (obtained from the total force F_x exerted by the fluid on the walls), the total suspension viscosity can be calculated as

$$\eta = \frac{\sigma_{xz}}{\dot{\gamma}} = \frac{F_x}{L_x L_y \dot{\gamma}} \tag{17}$$

Initial positions are calculated by using a pre-processing Monte-Carlo algorithm which assigns an appropriate potential $V(r)$ to every solid particle and therefore drives them to non-overlapping positions as explained in Ref. [53]. We have tested in specific situations the effect of the choice of different random initial conditions on the final results for the viscosity and have found no deviations for

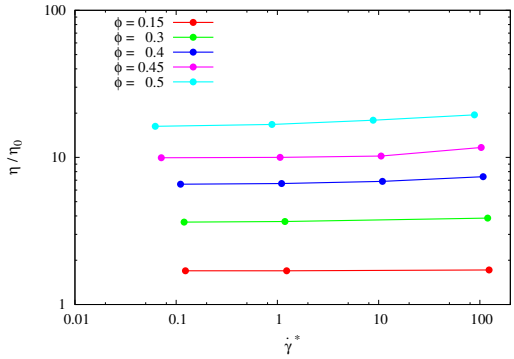

Figure 5: Viscosity of the suspension for different shear rates and concentrations.

the wall force data averaged once the system reached a stationary state.

Solvent viscosity η_0, speed of sound c_s as well as input shear rate $\dot{\gamma}^{in}$ are taken as in the previous section. Particle Reynolds number is fixed to $\mathrm{Re_p} = a^2\dot{\gamma}^{in}\rho_0/\eta_0 = 0.00625$. In order to study the rheology a dimensionless shear rate $\dot{\gamma}^* = \frac{6\eta_0 a\dot{\gamma}}{F_0}$ is defined [39], which is controlled by changing the amplitude F_0 of the repulsive force.

Results for the relative suspension viscosity $\eta_r = \eta/\eta_0$ have been drawn in Fig. 5 for different $\dot{\gamma}^*$. Parameter $\tau^{-1} = 0.001a$ in Eq. (8) has been chosen corresponding to a very short-range interparticle repulsion and mimicking the nearly hard-sphere case.

The behavior of the suspension is clearly Newtonian at low solid concentrations, up to $\phi \approx 0.3$. For larger concentration weak shear-thickening is observed, which remains however very mild up $\phi = 0.5$, with a modest maximal 10 % increase over three orders of magnitude in $\dot{\gamma}^*$. These results are in line with previous data obtained using Stokesian Dynamics simulations of bulk systems in Refs.[27, 32] and with our previous 2D simulations under very weak confinement (large Couette gap) [66]. In order to compare our data with available results in the literature, in figure 6 the dependence of the relative suspension viscosity η_r on the volume fraction ϕ is shown. Results are presented together with numerical data of Sierou and Brady [27] and the experimental data of Zarraga

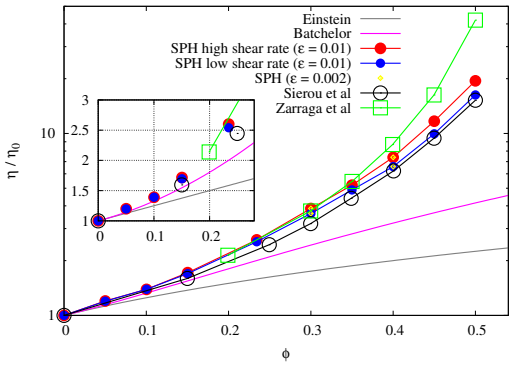

Figure 6: Relative viscosity vs volume fraction. Results of SPH are compared with the experiments by Zarraga et al [33] (□). and the simulations by Sierou et al [27] (◯). Low-shear rate (●) and large-shear rate (●) SPH viscosities from Fig. 5. Effect of smaller tolerance ϵ on convergence of the measured viscosity (●) is also shown . Einstein and Batchelor solutions [11, 67] valid in the dilute/semi-dilute regimes are shown in the inset.

et al. [33]. For sake of clearness, we reported only these two indicative set of measurements in figure 6, being the recent experimental results of Bertevas et al. [32] quasi overlapping with data from Ref.[33]. Moreover, numerical data of Sierou et al. show the largest viscosities and, to the best of our knowledge, they represent the set of simulation data which is currently closest to experimental values.

Two curves have been drawn from our SPH simulations corresponding, respectively, to the maximum and minimum viscosity values obtained at large and small applied shear rates. Strictly speaking, only values corresponding to the Newtonian plateau for every concentration are shear-rate independent and should be drawn in figure 6. However, for sake of completeness we reported both extremal values in order to visualize also the maximal measured deviations in the simulations. Moreover, maximal values within the shear-thickening regime were reported in the Sierou curve (see classical Fig. 2 in Ref.[27] - no Newtonian plateau was observed by the authors), and so do we too.

	Present work		exp		num	
ϕ	$\dot{\gamma}^* \approx 0.1$	$\dot{\gamma}^* \approx 100$	[33]	[35]	[27]	[32]
0.05	1.20	1.20	–	–	–	–
0.10	1.39	1.40	–	1.35	–	1.32
0.15	1.70	1.72	–	–	1.60	1.56
0.20	–	–	2.14	2.03	–	1.89
0.234	2.54	2.60	–	–	–	–
0.25	–	–	–	–	2.45	2.36
0.30	3.63	3.87	3.75	3.59	3.19	3.14
0.35	4.89	5.19	5.45	5.32	4.40	4.39
0.40	6.57	7.40	8.69	8.14	6.23	6.17
0.45	9.95	11.68	16.28	14.05	9.42	–
0.50	16.27	19.47	41.99	–	15.22	–

Table 1: Relative viscosity of current SPH simulations for several concentrations compared with previous experimental, (Zárraga et al. [33] and Tanner et al [35]) and numerical data (Sierou et al. [27] and Bertevas et al. [32]).

Before to discuss them, we should stress that these results are obtained with a SPH model which is tuning-parameter free. In fact, no calibration of particle radius based on Stokes flow (hydrodynamic radius) or radial distribution function needs to be done as in DPD [24, 68], LBM [18, 19] or in a recent grid-based method [69], but solid particle size is defined in terms of a precise prescription of the solid-liquid interface and therefore of geometrical radius a. This is particularly important when defining ϕ at large concentration, where estimates based on radii calibrated from single-sphere measurements in a dilute regime might be wrong.

In the dilute and semi-dilute regimes our data reproduce exactly the Einstein's solution for $\phi \leq 0.1$ [11] and high-order Batchelor's correction [67] (inset figure 6). For $\phi > 0.15$ deviations from analytical theories are evident. In the moderately dense and concentrated regime our data, compared to simula-

tions of Ref. [27] (black circles), are always larger, both in the shear-thickening (red circles) and low-shear Newtonian plateau (blue circles). Due to the vertical logarithmic scale the difference is more evident at $\phi = 0.3$ than at larger concentrations.

Compared to Ref. [33] (green squares), the current SPH results match experimental data up to $\phi \approx 0.35$, with large deviations in η_r still occurring at larger concentrations. This last discrepancy with experiments is present also in other numerical schemes and it might be due to the presence of interparticle contact forces, surface roughness or three-body lubrication effects which have not been included in the model.

It should be also stressed that these results are fully converged in terms of an ϵ analysis (see Sec. I.C). In fact two different tolerances $\epsilon = 0.01, 0.002$ in the semi-implicit lubrication iteration have been considered and the measured viscosities match fairly well at the two concentrations considered (see Fig. 6).

Moreover it should be remarked that confinement and finite size effects have been ruled out in our simulations. We have systematically checked that size of the system both, in the periodic direction (L_x, L_y) as well in the direction of confinement L_z are sufficiently large to deliver the converged results reported in Fig. 6.

Full set of data are presented in Table 1 and compared with numerical and experimental data. Although the deviations with simulation data of Sierou [27] are not significant, only ≈ 20 % at $\phi = 0.5$, (and they certainly do not explain the largest increase of η_r still observed experimentally), these are, to the best of our knowledge, the highest fully-converged viscosity values reported in the literature for hydrodynamically interacting non-colloidal suspensions.

It is worth to notice that a difference with previous numerical approaches [27, 32] lies in the evaluation of the suspension viscosity which is normally done via Irving-Kirkwood theory. Here, a wall-force based approach is considered instead which is closely related to the way viscosity is determined in experiments. In [20] the two approaches have been compared numerically showing excellent agreement, in such a way that we do not expect significant deviations associated

to the procedure adopted.

It should be also remarked that no particle-wall lubrication has been considered in this work. Introduction of this force could affect the suspension viscosity by effectively changing the "slip" occurring at the wall and therefore modifying the shear-rate defined in terms of wall velocities. On the other hand, similarly to experiments [2], we obtain here a corrected effective shear-rate by interpolating the linear velocity profile directly from the bulk, therefore ruling out systematically possible slip effects. As a consequence, we do not expect significant influence on our viscosity measurements.

3.2.1. Suspension microstructure

In order to understand the cause of the observed shear-thickening for this suspension, in this section we focus on the microstructure by analyzing the particle radial distribution function (RDF). In particular we investigate the influence of shear rate $\dot{\gamma}^*$ on the RDF along different planes. We focus on suspension at concentration $\phi = 0.4$ where mild, but visible, shear-thickening is observed in Fig. 5.

Fig. 7 shows respectively the RDF along the velocity/velocity-gradient plane xz (top figures), along the vorticity/velocity-gradient plane yz (middle figures) and along the velocity/vorticity plane xy (bottom figures) at three indicative shear rates $\dot{\gamma}^* \approx 1, 10, 100$. Consistently with established results for non-colloidal suspensions [2], the RDF in the shearing plane xz is shown to be anisotropic and fore-aft asymmetric indicating uneven probability for particle arrangements with areas of high probability in correspondence of strong boundary layers located along the compressive axis of shear and a depleted area in the recession quadrant (top).

The broken symmetry in the shearing plane is a direct consequence of short-range repulsive force, which slows down approaching and accelerates departing of any two nearby particles. This fore-and-aft asymmetry resembles Parsi&Gadala-Marias experimental measurements on a concentrated suspension of solid spheres [70] as well as recent experiments and simulations using Stokesian Dynamics

[30]. On the other hand, no particular structure is observed in the remaining planes, with an RDF isotropic indicating presence of a disordered-state for the solid particles at every shear rate investigated. Note that we did not observed

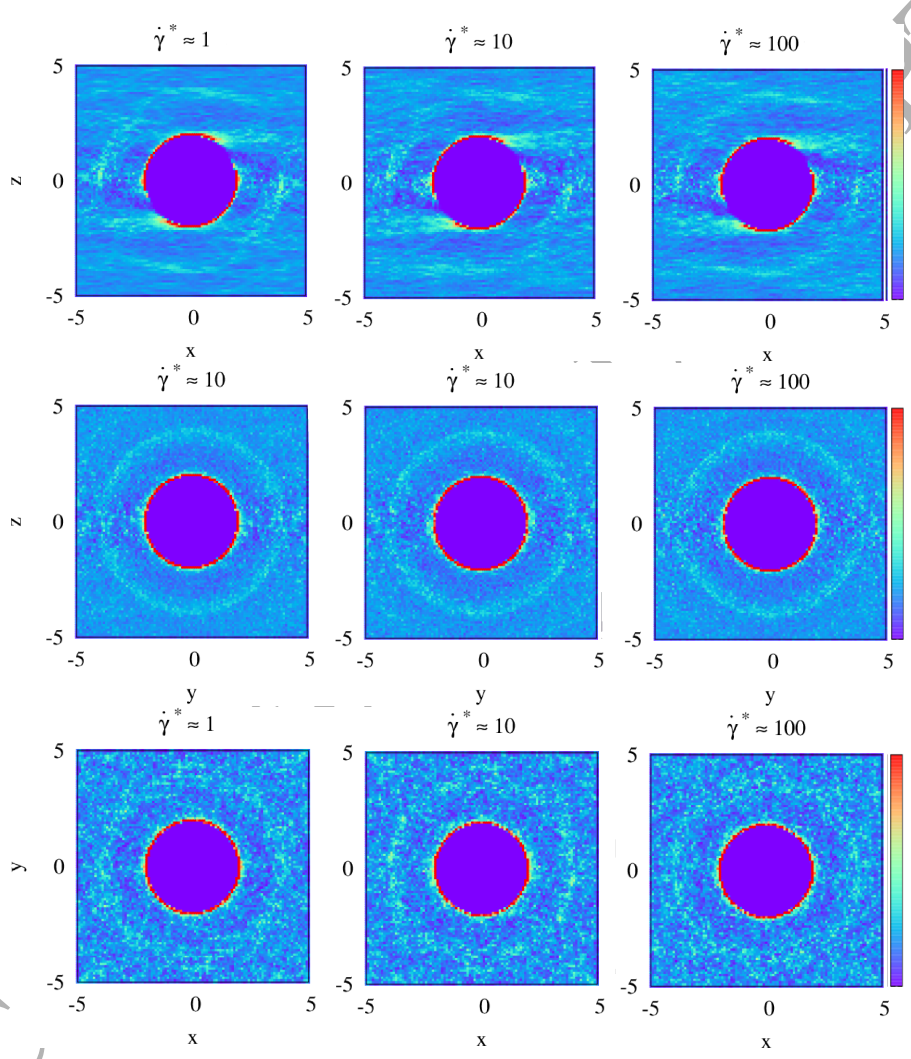

Figure 7: Radial distribution function for a sheared particle suspension at $\phi = 0.4$ with $\tau^{-1} = 0.001a$. Top figures show averaged RDF projected into different planes for different shear rates. Top: velocity/velocity-gradient plane xz. Middle: vorticity/velocity-gradient plane yz. Bottom: velocity/vorticity plane xy.

any asymmetry, i.e. weak particle chaining, in the vorticity direction as recently reported in SANS measurements of colloidal systems in [44].

Boundary layers and corresponding peak location in the xz-plane is completely determined by the balance of shearing and repulsive forces which is changed by the effective shear rate parameters $\dot{\gamma}^* = \frac{6\eta_0 a\dot{\gamma}}{F_0}$. For different values of $\dot{\gamma}^*$ balance will be reached at increasingly smaller interparticle distances, where lubrication forces are stronger and explain the increased viscosity. In [39, 28, 27] this explanation for the onset of shear-thickening has been pushed forward by contemplating the existence of finite regions of local high solid particle density, termed "hydroclusters". Upon increasing shear rate, convective forces dominate over entropic repulsive Brownian forces, being able to bring solid particles close together forming these transient hydrodynamic aggregates. In the thin gaps between multiple interacting particles inside hydroclusters, diverging lubrication forces are active which in turn induce even larger stresses in the system. The existence of hydroclusters was confirmed by experiments using flow-small angle neutron scattering [43, 42], optical methods including flow dichroism [41], fast confocal microscopy [40] and numerical simulations [39, 28, 27].

Although hydrocluster theory seems not be able to predict the large discontinuous shear-thickening observed in many experiments [71, 72, 73] - for which new interparticle modelling based on contact friction forces is emerging as novel paradigm [46, 45] - it was recently shown that continuous but significant shear-thickening can be still obtained in two-dimensional systems in presence of confinement [52].

Hydrodynamic cluster analysis: in this subsection we present an analysis of the suspension microstructure for hard spheres based on a cluster detection algorithm proposed in Ref.[66] for two-dimensional systems. The goal is to verify the existence of a detectable increased portion of hydroclusters which can be directly connected to the small shear-thickening observed in Fig. 5.

In order to detect a cluster, we take surface distance $0.001a$ as a threshold below which two particles are considered to be 'connected'. $N_{cluster}$ is defined

as the number of solid spheres inside every cluster and determines its size.

One-dimensional RDF of solid particles for a typical system with $\phi = 0.4$ are shown in Fig. 8 (top). As discussed above, the maximum probability peak moves towards smaller averaged interparticle gaps s for increasing shear rates, and consequently the role played by lubrication interaction becomes more relevant.

Probability distribution function (PDF) of cluster size are shown in Fig. 8 (bottom) for several applied shear rates. At low shear rates -corresponding to the Newtonian plateau of Fig.5 clusters of size $N_{cluster} \geq 1$ are barely formed. At the largest shear rate investigated $\dot{\gamma}^* = 100$, the tails of the PDF extend visibly indicating presence of larger aggregates through the domain in agreement

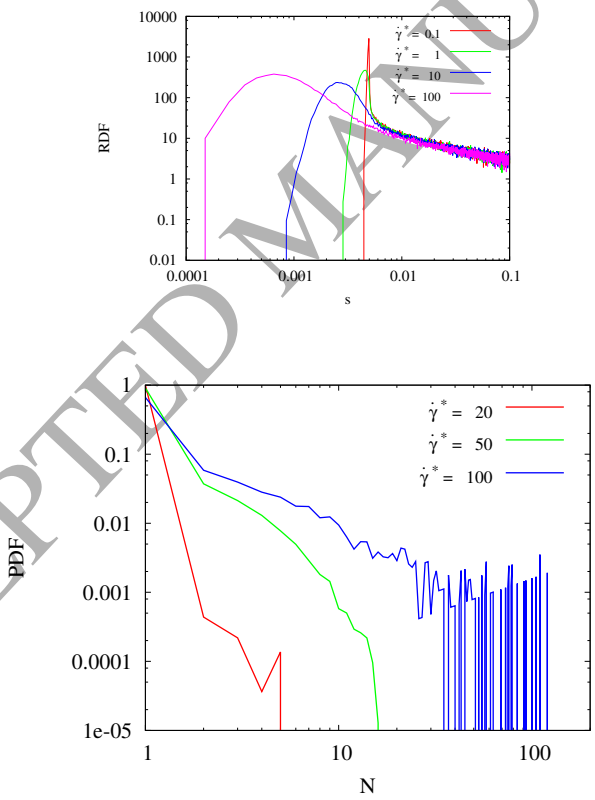

Figure 8: Top: one-dimensional RDF from the simulation of $\phi = 0.4$ at different shear rates. Bottom: PDF of hydroclusters size for $\phi = 0.4$ at different shear rates.

with experimental findings [40].

Similarly, an instantaneous real-space configuration of hydroclusters has been extracted from simulations and is shown in Fig. 9 for the shear-thickening regime ($\dot{\gamma}^* = 100$, blue curve in Fig. 8 (bottom)). Different colors indicate different cluster-size with smaller aggregates being depicted in transparent style for sake of clarity. The aggregates as well as their morphologies can be fully appreciated and exhibit qualitative similarities with the snapshots obtained form confocal movies in [40]. Similarly to what observed in [66], hydroclusters do represent truly transient aggregates varying continuously in size and location. With the same choice of the threshold distance only rare events with $N_{cluster} \approx 2-4$ could be detected at $\dot{\gamma}^* = 10$ and are not shown here.

It should be remarked that possible time-dependent behaviour in the build-up of microstructure could arise, which in turn can be related to rheological changes. Study of the rheology-microstructure link under transient flow condi-

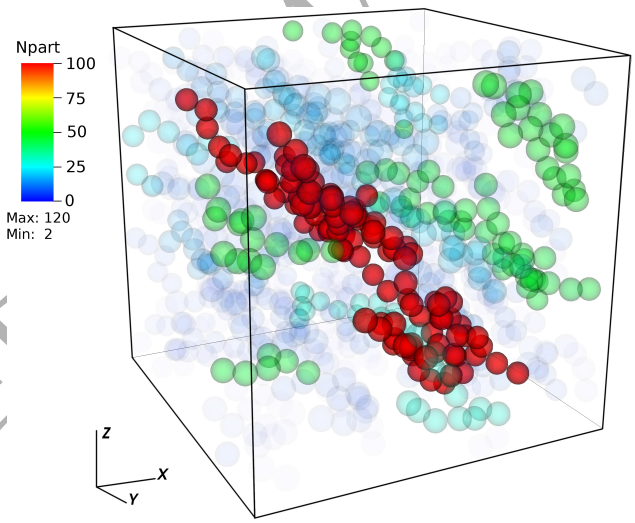

Figure 9: Snapshot of hydroclusters configuration for $\phi = 0.4$ and $\dot{\gamma}^* = 100$ corresponding to viscosity data shown in Fig. 5. Cluster detection was obtained by defining a minimal cutoff distance between suspended particles $R_c = 10^{-3}a$. With this choice for R_c only rare events with $N_{cluster} \approx 2-4$ could be detected at $\dot{\gamma}^* = 10$.

tions, e.g. start-up shear, will be a matter of future investigations.

4. Conclusions

In this work we have presented a Smoothed Particle Hydrodynamics model to study rheology and microstructure of a non-colloidal suspension of spherical particles in a Newtonian solvent. The splitting scheme presented in [52] is generalized to three-dimensions and interparticle normal/tangential lubrication forces are considered. Singular lubrication dynamics is calculated implicitly by solving analytically the two-body lubrication problem iteratively all over the pairs of suspended particles. In order to check the accuracy, the new model is first tested for the dynamics of two hydrodynamically-interacting spherical particles undergoing a shear flow. Rheology of a three-dimensional hard-spheres suspension confined in a plane Couette rheometer is investigated for solid volume fractions up to $\phi = 0.5$. We focus here specifically on the relative viscosity η_r where simulation data are analyzed against numerical convergence of the splitting scheme for the lubrication dynamics. Converged viscosity values are compared with available experimental and simulations data. Excellent agreement with experiments (within 5 %) is obtained up to concentrations $\phi = 0.35$ where a Newtonian plateau for η_r is observed over three order of magnitudes in the applied shear rate. These data confirm both experimental findings [33, 34, 35] and previous simulations [27, 32]. Viscosity data presented here, although showing slightly higher values with respect to numerical data reported previously in the literature, are still unable to explain the large relative viscosities observed experimentally.

Similar to previous calculations, modest shear-thickening (less than 10 % over three orders of magnitudes in the shear rate) is also observed which is related to anisotropy of the particle radial distribution function (RDF) and presence of reversible hydrodynamic aggregates increasing in size with increasingly applied shear rates, consistently with our previous two-dimensional results for non-frictional systems where small continuous shear-thickening was observed in

the case of weak confinement [66]. On the other hand, the strong discontinuous shear-thickening observed in some experiments appears not to be explained in terms of hydrodynamically-bound clusters only. This is also in agreement with experimental observations for colloidal systems in the Brownian-less limit -large Peclet numbers- [38, 40] but still in disagreement with the opposite weak shear-thinning reported in several non-colloidal suspensions [33, 34, 35, 9] for which a conclusive explanation is still missing. The results presented in this work - which are based on an alternative route to extract suspension viscosity via overall wall force measurement - confirm previous simulations data and indicate that the physics contained in a simple Newtonian-based lubrication interaction is not sufficient to describe the shear-thinning phenomenon in non-colloidal systems.

Incorporation of interparticle friction forces can provide a mechanism to increase the suspension viscosity, however there are some issues when applied to the specific problem of non-colloidal systems: (1) friction forces enhance shear-thickening and/or produce discontinuous shear-thickening [45, 46, 31] which is opposite to the shear-thinning observed in [33, 34, 35, 9]; (2) effect of the roughness in frictional models still does not match the experimental systems [48], i.e. unrealistic excessive roughness must be considered to obtain similar viscosity values. A similar argumentation holds also in the colloidal case where direct measurements of the friction at surfaces show extremely low coefficients compared to those assumed in simulations [44]. (3) Both quantitative (viscosity magnitudes) and qualitative (shear-thinning) deviations between simulation results and experimental data in non-colloidal systems appear already in the moderately dense case -i.e. for $\phi \leq 0.4$ - significantly below the jamming transition, where the system reaches frustration and frictional contacts are expected to dominate the dynamics. Further numerical analysis is therefore urgently required to clarify these discrepancies. In particular, we are currently investigating effects of weak non-Newtonian behaviour of the matrix, poly-dispersivity as well as confinement effects on the rheological behaviour reported in this work and results will be presented soon.

Acknowledgements

Computing time provided by HPC Wales via the project "Multiscale particle simulation for complex fluids" (Nr. HPCWT050) is gratefully acknowledged. Some figures were created utilizing VISIT software [74].

References

References

[1] R. I. Tanner, Engineering rheology, 2nd Edition, Oxford University Press New York, 2000.

[2] J. Mewis, N. J. Wagner, Colloidal Suspension Rheology, Cambridge University Press, 2011, cambridge Books Online.

[3] K. Leontaritis, G. Mansoori, et al., Asphaltene flocculation during oil production and processing: A thermodynamic collodial model, in: SPE International Symposium on Oilfield Chemistry, Society of Petroleum Engineers, 1987.

[4] G. Maitland, Oil and gas production, Current opinion in colloid & interface science 5 (5) (2000) 301–311.

[5] Y. Lee, E. Wetzel, N. Wagner, The ballistic impact characteristics of kevlar woven fabrics impregnated with a colloidal shear thickening fluid, Journal of Materials Science 38 (13) (2003) 2825–2833.

[6] N. J. Wagner, J. F. Brady, Shear thickening in colloidal dispersions, Physics Today 62 (10) (2009) 27–32.

[7] L. Isa, R. Besseling, A. N. Morozov, W. C. K. Poon, Velocity oscillations in microfluidic flows of concentrated colloidal suspensions, Phys. Rev. Lett. 102 (2009) 058302.

[8] A. I. Campbell, M. D. Haw, Jamming and unjamming of concentrated colloidal dispersions in channel flows, Soft Matter 6 (2010) 4688–4693.

[9] Y. Lin, G. W. H. Tan, N. Phan-Thien, B. C. Khoo, Flow enhancement in pulsating flow of non-colloidal suspensions in tubes, Journal of Non-Newtonian Fluid Mechanics 212 (2014) 13 – 17.

[10] J. A. Lewis, Direct-write assembly of ceramics from colloidal inks, Current Opinion in Solid State and Materials Science 6 (3) (2002) 245 – 250.

[11] A. Einstein, Eine neue bestimmung der molekldimensionen, Annalen der Physik 324 (2) (1906) 289–306.

[12] A. Einstein, Berichtigung zu meiner arbeit: "eine neue bestimmung der molekü ldimensionen", Annalen der Physik 339 (3) (1911) 591–592.

[13] G. Batchelor, J.-T. Green, The hydrodynamic interaction of two small freely-moving spheres in a linear flow field, Journal of Fluid Mechanics 56 (02) (1972) 375–400.

[14] D. Bedeaux, R. Kapral, P. Mazur, The effective shear viscosity of a uniform suspension of spheres, Physica A: Statistical Mechanics and its Applications 88 (1) (1977) 88 – 121.

[15] D. Quemada, Rheology of concentrated disperse systems and minimum energy dissipation principle, Rheologica Acta 16 (1) (1977) 82–94.

[16] W. R. Hwang, M. A. Hulsen, H. E. Meijer, Direct simulation of particle suspensions in sliding bi-periodic frames, Journal of Computational Physics 194 (2) (2004) 742 – 772.

[17] G. DAvino, P. Maffettone, M. Hulsen, G. Peters, A numerical method for simulating concentrated rigid particle suspensions in an elongational flow using a fixed grid, Journal of Computational Physics 226 (1) (2007) 688 – 711.

[18] A. Ladd, R. Verberg, Lattice-boltzmann simulations of particle-fluid suspensions, Journal of Statistical Physics 104 (5-6) (2001) 1191–1251.

[19] N.-Q. Nguyen, A. Ladd, Lubrication corrections for lattice-boltzmann simulations of particle suspensions, Physical Review E 66 (4) (2002) 046708.

[20] N. Phan-Thien, N. Mai-Duy, B. C. Khoo, A spring model for suspended particles in dissipative particle dynamics, Journal of Rheology 58 (4) (2014) 839–867.

[21] N. Mai-Duy, N. Phan-Thien, B. Khoo, Investigation of particles size effects in dissipative particle dynamics (dpd) modelling of colloidal suspensions, Computer Physics Communications 189 (2015) 37 – 46.

[22] S. Jamali, M. Yamanoi, J. Maia, Bridging the gap between microstructure and macroscopic behavior of monodisperse and bimodal colloidal suspensions, Soft Matter 9 (2013) 1506–1515.

[23] S. Jamali, A. Boromand, N. Wagner, J. Maia, Microstructure and rheology of soft to rigid shear-thickening colloidal suspensions, Journal of Rheology 59 (6) (2015) 1377–1395.

[24] W. Pan, B. Caswell, G. E. Karniadakis, Rheology, microstructure and migration in brownian colloidal suspensions, Langmuir 26 (1) (2009) 133–142.

[25] G. Bossis, J. F. Brady, The rheology of brownian suspensions, The Journal of chemical physics 91 (3) (1989) 1866–1874.

[26] A. Sierou, J. F. Brady, Accelerated stokesian dynamics simulations, Journal of Fluid Mechanics 448 (2001) 115–146.

[27] A. Sierou, J. Brady, Rheology and microstructure in concentrated noncolloidal suspensions, Journal of Rheology 46 (5) (2002) 1031–1056.

[28] D. R. Foss, J. F. Brady, Structure, diffusion and rheology of brownian suspensions by stokesian dynamics simulation, Journal of Fluid Mechanics 407 (2000) 167–200.

[29] J. W. Swan, J. F. Brady, Simulation of hydrodynamically interacting particles near a no-slip boundary, Physics of Fluids 19 (11) (2007) –.

[30] F. Blanc, E. Lemaire, A. Meunier, F. Peters, Microstructure in sheared non-brownian concentrated suspensions, Journal of Rheology 57 (1) (2013) 273–292.

[31] R. Mari, R. Seto, J. F. Morris, M. M. Denn, Shear thickening, frictionless and frictional rheologies in non-brownian suspensions, Journal of Rheology (1978-present) 58 (6) (2014) 1693–1724.

[32] E. Bertevas, X. Fan, R. I. Tanner, Simulation of the rheological properties of suspensions of oblate spheroidal particles in a newtonian fluid, Rheologica acta 49 (1) (2010) 53–73.

[33] I. E. Zarraga, D. A. Hill, D. T. Leighton Jr, The characterization of the total stress of concentrated suspensions of noncolloidal spheres in newtonian fluids, Journal of Rheology 44 (2) (2000) 185–220.

[34] A. Singh, P. R. Nott, Experimental measurements of the normal stresses in sheared stokesian suspensions, Journal of Fluid Mechanics 490 (2003) 293–320.

[35] R. I. Tanner, F. Qi, S. Dai, Scaling the normal stresses in concentrated non-colloidal suspensions of spheres, Rheologica Acta 52 (4) (2013) 291–295.

[36] F. Ferrini, D. Ercolani, B. de Cindio, L. Nicodemo, L. Nicolais, S. Ranaudo, Shear viscosity of settling suspensions, Rheologica Acta 18 (2) (1979) 289–296.

[37] F. GadalaMaria, A. Acrivos, Shearinduced structure in a concentrated suspension of solid spheres, Journal of Rheology 24 (6) (1980) 799–814.

[38] C. D. Cwalina, N. J. Wagner, Material properties of the shear-thickened state in concentrated near hard-sphere colloidal dispersions, Journal of Rheology 58 (4) (2014) 949–967.

[39] J. F. Brady, G. Bossis, The rheology of concentrated suspensions of spheres in simple shear flow by numerical simulation, Journal of Fluid Mechanics 155 (1985) 105–129.

[40] X. Cheng, J. H. McCoy, J. N. Israelachvili, I. Cohen, Imaging the microscopic structure of shear thinning and thickening colloidal suspensions, Science 333 (6047) (2011) 1276–1279.

[41] J. Bender, N. J. Wagner, Reversible shear thickening in monodisperse and bidisperse colloidal dispersions, Journal of Rheology 40 (5) (1996) 899–916.

[42] B. J. Maranzano, N. J. Wagner, Flow-small angle neutron scattering measurements of colloidal dispersion microstructure evolution through the shear thickening transition, The Journal of Chemical Physics 117 (22) (2002) 10291–10302.

[43] H. M. Laun, R. Bung, S. Hess, W. Loose, O. Hess, K. Hahn, E. Hadicke, R. Hingmann, F. Schmidt, P. Lindner, Rheological and small angle neutron scattering investigation of shear-induced particle structures of concentrated polymer dispersions submitted to plane poiseuille and couette flow), Journal of Rheology 36 (4) (1992) 743–787.

[44] A. K. Gurnon, N. J. Wagner, Microstructure and rheology relationships for shear thickening colloidal dispersions, Journal of Fluid Mechanics 769 (2015) 242–276.

[45] N. Fernandez, R. Mani, D. Rinaldi, D. Kadau, M. Mosquet, H. Lombois-Burger, J. Cayer-Barrioz, H. J. Herrmann, N. D. Spencer, L. Isa, Microscopic mechanism for shear thickening of non-brownian suspensions, Phys. Rev. Lett. 111 (2013) 108301.

[46] R. Seto, R. Mari, J. F. Morris, M. M. Denn, Discontinuous shear thickening of frictional hard-sphere suspensions, Phys. Rev. Lett. 111 (2013) 218301.

[47] S. Gallier, E. Lemaire, F. Peters, L. Lobry, Rheology of sheared suspensions of rough frictional particles, Journal of Fluid Mechanics 757 (2014) 514–549.

[48] J. Y. Moon, S. Dai, L. Chang, J. S. Lee, R. I. Tanner, The effect of sphere roughness on the rheology of concentrated suspensions, Journal of Non-Newtonian Fluid Mechanics 223 (2015) 233–239.

[49] J. J. Monaghan, Smoothed particle hydrodynamics, Reports on progress in physics 68 (8) (2005) 1703.

[50] I. Sbalzarini, J. Walther, M. Bergdorf, S. Hieber, E. Kotsalis, P. Koumoutsakos, {PPM} a highly efficient parallel particlemesh library for the simulation of continuum systems, Journal of Computational Physics 215 (2) (2006) 566 – 588.

[51] X. Bian, S. Litvinov, R. Qian, M. Ellero, N. A. Adams, Multiscale modeling of particle in suspension with smoothed dissipative particle dynamics, Physics of Fluids 24 (1) (2012) 012002.

[52] X. Bian, M. Ellero, A splitting integration scheme for the sph simulation of concentrated particle suspensions, Computer Physics Communications 185 (1) (2014) 53–62.

[53] A. Vázquez-Quesada, X. Bian, M. Ellero, Three-dimensional simulations of dilute and concentrated suspensions using smoothed particle hydrodynamics, Computational Particle Mechanics (2015) 1–12.

[54] P. Español, M. Revenga, Smoothed dissipative particle dynamics, Physical Review E 67 (2) (2003) 026705.

[55] A. Vázquez-Quesada, M. Ellero, P. Español, Consistent scaling of thermal fluctuations in smoothed dissipative particle dynamics, The Journal of chemical physics 130 (3) (2009) 034901.

[56] A. Vázquez-Quesada, M. Ellero, P. Español, A sph-based particle model for computational microrheology, Microfluidics and nanofluidics 13 (2) (2012) 249–260.

[57] A. Vázquez-Quesada, M. Ellero, P. Español, Smoothed particle hydrodynamic model for viscoelastic fluids with thermal fluctuations, Physical Review E 79 (5) (2009) 056707.

[58] X. Hu, N. Adams, Angular-momentum conservative smoothed particle dynamics for incompressible viscous flows, Physics of Fluids 18 (10) (2006) 101702.

[59] J. P. Morris, P. J. Fox, Y. Zhu, Modeling low reynolds number incompressible flows using sph, Journal of computational physics 136 (1) (1997) 214–226.

[60] M. Ellero, N. A. Adams, Sph simulations of flow around a periodic array of cylinders confined in a channel, International Journal for Numerical Methods in Engineering 86 (8) (2011) 1027–1040.

[61] J. J. Monaghan, Simulating free surface flows with sph, Journal of computational physics 110 (2) (1994) 399–406.

[62] S. Kim, S. J. Karrila, Microhydrodynamics: principles and selected applications, 1991.

[63] D. Jeffrey, Y. Onishi, Calculation of the resistance and mobility functions for two unequal rigid spheres in low-reynolds-number flow, Journal of Fluid Mechanics 139 (1984) 261–290.

[64] D. Dratler, W. Schowalter, Dynamic simulation of suspensions of non-brownian hard spheres, Journal of Fluid Mechanics 325 (1996) 53–77.

[65] J. F. Brady, J. F. Morris, Microstructure of strongly sheared suspensions and its impact on rheology and diffusion, Journal of Fluid Mechanics 348 (1997) 103–139.

[66] X. Bian, S. Litvinov, M. Ellero, N. J. Wagner, Hydrodynamic shear thickening of particulate suspension under confinement, Journal of Non-Newtonian Fluid Mechanics 213 (2014) 39–49.

[67] G. Batchelor, J.-T. Green, The determination of the bulk stress in a suspension of spherical particles to order c^2, Journal of Fluid Mechanics 56 (03) (1972) 401–427.

[68] N. Phan-Thien, N. Mai-Duy, B. C. Khoo, A spring model for suspended particles in dissipative particle dynamics, Journal of Rheology 58 (4) (2014) 839–867.

[69] A. Vázquez-Quesada, F. B. Usabiaga, R. Delgado-Buscalioni, A multiblob approach to colloidal hydrodynamics with inherent lubrication, The Journal of chemical physics 141 (20) (2014) 204102.

[70] F. Parsi, F. GadalaMaria, Foreandaft asymmetry in a concentrated suspension of solid spheres, Journal of Rheology 31 (8) (1987) 725–732.

[71] A. Fall, N. Huang, F. Bertrand, G. Ovarlez, D. Bonn, Shear thickening of cornstarch suspensions as a reentrant jamming transition, Phys. Rev. Lett. 100 (2008) 018301.

[72] E. Brown, N. A. Forman, C. S. Orellana, H. Zhang, B. W. Maynor, D. E. Betts, J. M. DeSimone, H. M. Jaeger, Generality of shear thickening in dense suspensions, Nat Mater 9 (3) (2010) 220–224.

[73] E. Brown, H. M. Jaeger, The role of dilation and confining stresses in shear thickening of dense suspensions, Journal of Rheology 56 (4) (2012) 875–923.

[74] H. Childs, E. Brugger, B. Whitlock, J. Meredith, S. Ahern, D. Pugmire, K. Biagas, M. Miller, C. Harrison, G. H. Weber, H. Krishnan, T. Fogal, A. Sanderson, C. Garth, E. W. Bethel, D. Camp, O. Rübel, M. Durant, J. M. Favre, P. Navrátil, Visit: An end-user tool for visualizing and analyzing very large data, in: High Performance Visualization–Enabling Extreme-Scale Scientific Insight, 2012, pp. 357–372.